OPTICS

Attosecond metrology in a continuous-beam transmission electron microscope

A. Ryabov[1,2], J. W. Thurner[2], D. Nabben[1], M. V. Tsarev[2]*, P. Baum[1,2]*

Electron microscopy can visualize the structure of complex materials with atomic and subatomic resolution, but investigations of reaction dynamics and light-matter interaction call for time resolution as well, ideally on a level below the oscillation period of light. Here, we report the use of the optical cycles of a continuous-wave laser to bunch the electron beam inside a transmission electron microscope into electron pulses that are shorter than half a cycle of light. The pulses arrive at the target at almost the full average brightness of the electron source and in synchrony to the optical cycles, providing attosecond time resolution of spectroscopic features. The necessary modifications are simple and can turn almost any electron microscope into an attosecond instrument that may be useful for visualizing the inner workings of light-matter interaction on the basis of the atoms and the cycles of light.

INTRODUCTION

Atoms and electrons move on femtosecond and attosecond time scales when driven from initial to final configurations in processes such as chemical reactions, phase transformations, electronic device operations, or optical transformations of light. A direct visualization of the atomistic origin of functionality in complex materials therefore calls for ultrafast imaging methods that resolve atomic and electronic motion on the level of the particles and their innate reaction rates. Ultrafast electron microscopy and diffraction in pump-probe geometry (1, 2) can resolve structural dynamics (3–5) and propagation of light intensities and near fields (6–8) with femtosecond time resolution, in part with sensitivity to electromagnetic field vectors (9, 10), but the basic phenomena in optics, nanophotonics, or metamaterials unfold on attosecond time scales (11, 12), shorter than a cycle of light. Researchers therefore aim at creating electron pulses of sub–light cycle duration (4, 13–15) for uniting electron microscopy and diffraction with attosecond science (12) to enable a direct visualization of the electromagnetic origin of light-matter interaction on fundamental dimensions in space and time. Although pioneering results have been achieved with photoemitted electron pulses and compression into attosecond bursts (13–15), the beams from these sources lack by a thousand to a million times the necessary electron current, emittance, and average brightness that would be needed for applications (12–17). A versatile electron microscopy that can visualize the foundations of light-matter interaction in complex materials on subwavelength and subcycle dimensions therefore remains to be established.

RESULTS

Here, we report the combination of a transmission electron microscope (TEM) with a continuous-wave laser that modulates the continuous electron beam into pulses that are shorter than half a cycle of light. Figure 1 depicts our concept and experiment. Our prototypical attosecond transmission electron microscope (A-TEM) uses an electron energy of $E_0 = 120$ keV and a continuous-wave laser with a wave-

length of $\lambda = 1950$ nm. To directly use the laser's electric field cycles (18) and not the cycle-averaging ponderomotive forces (19) for electron-beam control, we place a planar dielectric membrane at the laser-electron intersection region through an access port that usually holds a condenser aperture (see Materials and Methods). The membrane material, 50 nm of boron-doped silicon, is thin enough to transmit the electrons and the laser light with almost no absorption losses and therefore withstands high levels of power and current. Yet, the membrane is thick enough to change the optical phase of the continuous laser wave upon transmission, thereby disrupting the symmetry of the oscillating Lorentz forces that would cancel out in a free-space interaction (20, 21). Because of the membrane, electrons that traverse
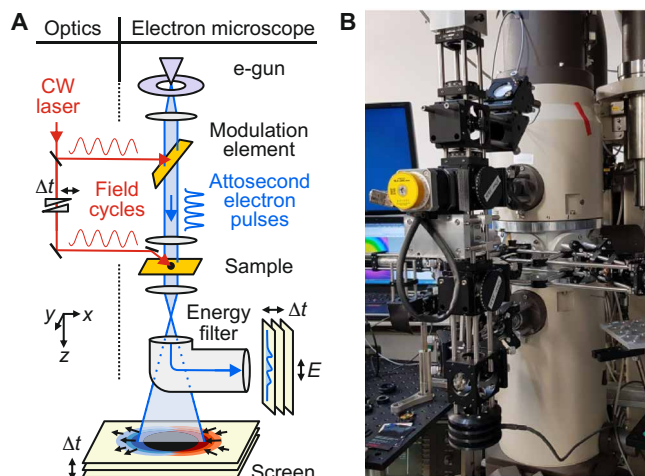

Fig. 1. Concept and experiment for attosecond-resolution electron microscopy. (**A**) The optical cycles of a continuous-wave (CW) laser (red) modulate the continuous electron beam (blue) of a TEM into a sequence of sub–light cycle pulses that are synchronized to a second light wave on the sample (yellow). Diagnostics of energy spectra as a function of the delay time Δt between the two laser waves reveal the pulse duration and quantum-coherent nature of the modulation. Optionally, delay-dependent real-space imaging (dotted blue line) can reveal electromagnetic phenomena in space and time. E, energy; e-gun, electron source. (**B**) Picture of the experiment. No femtosecond laser or modification of the electron source (dark gray) is required to transform an electron microscope into an attosecond instrument. Photo credit: A. Ryabov, Ludwig-Maximilians-Universität München and Universität Konstanz.

[1]Universität Konstanz, Universitätsstr. 10, 78464 Konstanz, Germany. [2]Ludwig-Maximilians-Universität München, Am Coulombwall 1, 85748 Garching, Germany.
*Corresponding author. Email: peter.baum@uni-konstanz.de (P.B.); maxim.tsarev@lmu.de (M.V.T.)

the optical focus region obtain from the symmetry-broken laser field cycles a net momentum kick as a function of their arrival time. In this way, the matter wave of electrons at a carrier frequency of ~10^{19} Hz is modulated by the cycles of laser light at a frequency of ~10^{14} Hz in a similar way as in radio communication, but a billion times faster. After some propagation, faster and slower electrons catch up with each other, and the beam therefore converts into an endless sequence of ultrashort electron pulses that have a spacing and timing that is dictated by the optical cycles of the laser wave (13, 14).

For electron pulse characterization, we place a second laser-driven dielectric membrane in between the microscope's twin lens at a ~12-cm distance from the first interaction. This second branch of the continuous-wave laser beam is guided into the microscope via a nonmagnetic steering mirror that is attached to one of the twin-lens surfaces (see Materials and Methods). With the help of a magnetic energy spectrometer (GIF 100, Gatan Inc.), we record the electron beam's final longitudinal momentum modulation after the dual laser interaction as a function of the time delay Δt between the two laser waves. Experiments with femtosecond lasers have established such quantum state tomography as a viable and sensitive method for attosecond electron pulse characterization (13).

Decisive for the energetic evidences of our intended pulse formation will be the question of whether our electrons are approximately point particles or rather coherent quantum wave packets that cover multiple cycle periods of the light wave. Pan et al. (22) and Kirchner et al. (20) have studied these cases and the transitional regime by simulations. For coherent electron wave packets, we can expect energy sidebands at multiples of the laser's photon energy $h\nu$ (6, 23), where $\nu = c/\lambda$ is the laser frequency because of constructive or destructive interferences of the energy modulations from adjacent optical cycles. All spectroscopic experiments with femtosecond pulses (6–8, 23) have so far produced such a discrete comb of photon-order sidebands because the laser-emitted electrons from a femtosecond source seem to have a wave packet duration exceeding tens of femtoseconds and therefore cover multiple cycles (24). In contrast, we use here spontaneously released electrons from a continuous thermal emitter at a measured energy bandwidth of $\sigma_E < 0.28$ eV (root mean square). The uncertainty principle $\sigma_t \sigma_E \geq \hbar/2$, where σ_t is the wave packet duration in the time domain, demands $\sigma_t \geq 1.2$ fs (root mean square), which is potentially much shorter than one optical cycle period (6.5 fs). If these quasi-point particles are injected in the form of compressed pulses into the optical cycles of the characterization laser, then we can expect a classical, sinusoidal displacement of the entire spectrum without quantum interferences, such as observed in terahertz experiments (25).

Figure 2A depicts the experimental results. Plotted is the final energy spectrum after the dual laser interaction as a function of the delay between the two coherent laser waves. We see that, at certain delays, the spectrum is shifted to lower energies ($\Delta t \approx -2$ fs), shifted to higher energies ($\Delta t \approx 2$ fs), broadened ($\Delta t \approx 3.5$ fs), or narrowed almost back to the original width ($\Delta t \approx 0$ fs). Wherever the spectrum is broadened, the central part decays in peak intensity. The data are periodic in time with $\lambda/c = 6.5$ fs, but the pattern is asymmetric in energy (see dotted lines). The highest energy changes that are newly generated around $\Delta E = \pm 1$ eV show substantial delays with respect to the minima at $\Delta E = 0$ eV.

The appearance of this time-modulated data shows that our continuous electron beam is compressed into a continuous sequence of ultrashort electron pulses that arrive at target in temporal synchrony

to the optical cycles, as intended. However, the pattern resembles neither a classical modulation of point particles (9, 18, 25) nor a quantum-mechanical picture with recognizable photon-order sidebands (6, 23). However, the result is compatible with an initial electron wave function that covers more than one optical cycle if we consider the technical noise of the acceleration voltage and the limited energy resolution of our spectrometer (see Materials and Methods). Figure 2B shows the results of a one-dimensional quantum-mechanical simulation (26) in which we transform the wave function into the electron rest frame, modulate the forward momentum, use a free-space time propagation operator to pass the electrons to the second interaction, apply a momentum modulation again, transform the results back to the laboratory frame, and calculate the energy spectrum by Fourier transformation. The result is convoluted with the measured energy spectrum at no modulation as an estimation of the technical fluctuations. The three sole fitting parameters are the optical intensities at the two modulation membranes and the absolute phase delay of the optical interferometer. The simulation results are shown in Fig. 2B and reproduce the measured data of Fig. 2A with all of its features.

For further analysis, we deconvolute the raw data of Fig. 2A with a Lucy-Richardson algorithm (see Materials and Methods). The reference spectrum, plotted in Fig. 2C in black, is the zero-loss peak of the direct beam without any laser modulation but with all modulation membranes in the beam. Laser-modulated raw data with its slight shoulders are plotted as the dashed line, and the green line shows the deconvolution result. We see a zero-loss peak at $\Delta E = 0$ eV and two sideband peaks at energies close to $h\nu = \pm 0.64$ eV. Higher-order sidebands are not exposed. Note that the deconvoluted energy widths are arbitrary but the feature positions and intensities are well defined (see Materials and Methods). Figure 2D shows the continuous electron currents in the zero-loss peak (red) and sidebands (blue, magenta) as a function of Δt. The solid lines are the results of the quantum simulations before applying the technical noise. We see a drop of the zero-loss peak by up to 30% and an increase of the sidebands by up to 20% at time delays of $\Delta t_{SB} \approx \pm 0.8$ fs (see dotted lines). The agreement of these results to the quantum mechanical sideband simulations shows that the continuous-wave laser indeed modulates the electron de Broglie wave from our thermal source in an at least partially coherent way. Figure 2E shows the sideband currents as a function of laser polarization. The modulation strength is maximum for p-polarization (90°) and diminishes for s-polarization (0°) because no effective changes of forward momentum are possible when there are no electric field components in propagation direction of the electrons (21, 24). Figure 2F shows the sideband currents as a function of laser power. In femtosecond experiments (6, 23), the nth-order sideband intensity is given by Bessel functions $J_n^2(g)$, where g is proportional to the optical modulation field. At small g, $J_{\pm1}^2(g) \approx \frac{1}{4}g^2$ and $J_0^2(g) \approx 1 - \frac{1}{2}g^2$. The observed linear scaling with laser power (proportional to g^2) therefore demonstrates that our endless electrons indeed interact directly with the continuous-wave laser's field cycles and not with ponderomotive forces (15, 19). Figure 2G depicts the measured attosecond delay of the first-order sidebands with respect to the timing of the zero-loss peak as a function of laser power at the compression. Although the duration of the compressed electron pulses changes substantially, the measured sideband delay remains almost constant. The value and precision of $\Delta t_{SB} = 810 \pm 27$ as (dashed line) indicate the temporal resolution that is enabled by our compression concept in spectroscopy; the measured Δt_{SB} is about two times smaller than the classical arrival time differences between point particles at $\pm h\nu$.
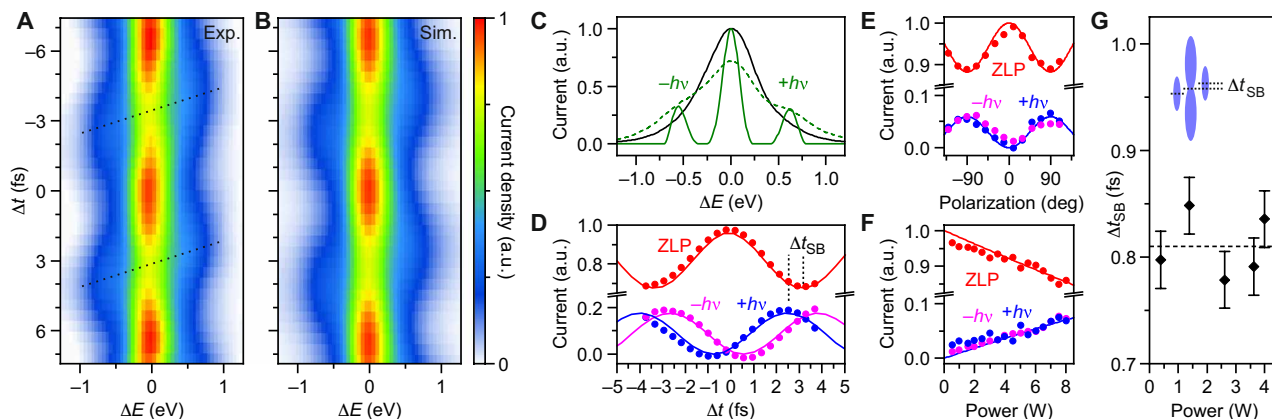
Fig. 2. Experimental results in comparison to simulations. (**A**) Measured energy spectrum as a function of time delay Δt. a.u., arbitrary units. (**B**) Result of a one-dimensional simulation, convoluted with the measured beam bandwidth. (**C**) Measured energy spectrum of the electron beam without modulation (black), with continuous-wave modulation (green, dashed), and after deconvolution (green). There are two sidebands appearing at $\pm h\nu$, the photon energy. (**D**) Beam current in the sidebands as a function of delay time. Dots are measurements and lines are quantum simulations. ZLP, zero-loss peak; Δt_{SB}, delay between the different photon orders. (**E**) Beam current in the sidebands as a function of laser polarization at the metrology membrane; compression is turned off. Dots are measurements and solid lines are $\cos^2$ fits. (**F**) Beam current in the sidebands as a function of laser power at the sample; the compression is turned off. Dots are measurements and lines are quantum simulations. (**G**) Measured delay (dots) of the $\pm$1st sideband maxima with respect to the dip of the zero-loss peak. Dashed line, average; inset, definition of Δt_{SB}.

The match of all measured data in Fig. 2 to the quantum simulations allows to extract an electron pulse duration in our A-TEM of $\tau \approx 0.9 \pm 0.3$ fs (root mean square) or 2.4 ± 0.7 fs (full width at half maximum) above a time-independent background current of ~30% that is caused by the decompressing optical half cycles (*13, 14*). These pulse durations are upper limits due to potential mechanical instabilities of our interferometric setup (see Fig. 1B) and the temporal distortions of the magnetic lenses (*27*). Nevertheless, the compressed electron pulses are substantially shorter than half an optical cycle of our laser light (3.3 fs) and therefore suitable for space-time imaging or energy loss spectroscopy of subcycle light-wave phenomena in a TEM. Shorter electron pulses with lower background current can be obtained with higher electron energies and a shorter distance between the two laser interactions. For example, 300-as pulses (root mean square above background) will be obtained for $E_0 = 200$ keV, $\lambda = 1.95$ μm, and $d = 9$ cm at a background current of <10%. Multi-color laser fields can further improve the compression by linearizing the time-dependent acceleration. The compressed electrons arrive at target at a repetition rate of $c/\lambda \approx 150$ THz and with <10^{-3} electrons per optical cycle, so space charge effects are negligible.

Emittance and brightness are the most decisive beam parameters in electron microscopy for practical imaging and spectroscopy applications but limited in femtosecond experiments by the laser repetition rate and space charge effects at the photoelectric emission (*28*). In contrast, the reported continuous-wave laser modulation provides, at the sample, a pulsed electron beam of almost the same electron current and average brightness as in nonpulsed operation because the laser controls the electron beam only after its formation at high energy and not by interaction with an electron-emitting material (*1*). Almost all electrons that pass through the laser focus are compressed in time. The data in Fig. 2 have been obtained with a beam current below 10 pA at <10^8 electrons per second to not saturate the zero-loss peak, but ~10^{11} pulsed electrons per second will be generated with a 20-nA beam from a modern field emitter source. These average beam currents are thousand to million times larger than in ultrafast electron microscopy with femtosecond sources (*1, 29*) and therefore useful for visualizing

electromagnetic phenomena at the frequency of light via field-vector imaging (*9*) or electron energy losses (*6*) at an unprecedented signal-to-noise ratio.

As a first spectroscopic application, we report an anomalous sideband-order peak shift in photon-induced near-field electron microscopy (*6*) and use this effect to measure the temporal coherence of thermally emitted electrons from a hot electron gas in a metal, the LaB_6 crystal of our electron emitter. Figure 3A shows one optical cycle of the data of Fig. 2A after deconvolution. To our surprise, the energies of the first and negative first photon–order sidebands deviate from their nominal positions at $\pm h\nu$ as a function of time, evident in tilts of the sideband features and shifts of the zero-loss peak with Δt. These anomalous photon-order peak shifts (POPS) disagree with previously reported femtosecond results (*6, 23*) in violating the conservation of photon energy; chirped electron pulses can only shift all sidebands in synchrony (*7, 20*). We can track the observations back to the limited temporal coherence of our continuous electron beam in combination with the huge time delay between our two interactions, >30 times larger than in femtosecond experiments (*13, 14*). Figure 3C depicts, in the upper part, an electron wave function (yellow) of limited temporal coherence and finite energy bandwidth of which the initial laser-electron interaction (blue arrows) has prepared sideband copies with equal phase fronts (gray lines). Propagation to the second interaction (lower part) induces nonlinear dispersion (gray lines), exaggerated in the figure. The characterization laser (magenta arrows) coherently couples the zero-loss peak with the sidebands for a second time, but now asymmetrically with respect to the central energy. In the depicted case, sideband population is coherently added at $|E - E_0| > h\nu$ (solid arrows) and coherently reduced at $|E - E_0| < h\nu$ (dotted arrows). Different Δt produce different sideband peak shifts, and the corresponding asymmetric depletions of the zero-loss peak move its position as well (see the solid line in Fig. 3A).

The strength of the POPS effect depends on the wave packet duration of the beam electrons before compression. Figure 3B shows simulated peak shifts for initial electron wave packet durations of
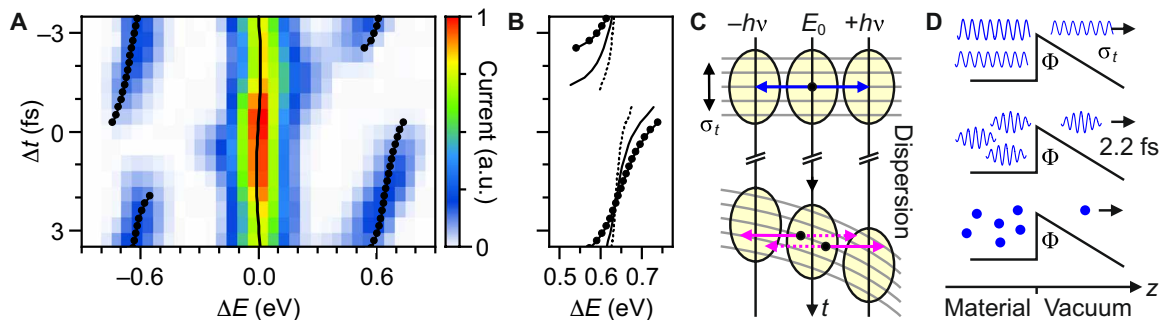
Fig. 3. Anomalous photon-order peak shifts and evidence for a finite spatiotemporal coherence of hot charge carriers in a metal. (**A**) Deconvoluted measurement data. Solid line, simulated peak shift of the zero-loss peak; big dots, simulated peak shifts of the sidebands. (**B**) Simulated sideband peak shifts for different electron wave packet lengths. Dashed line, 4.3 fs; solid line, 2.7 fs; big dots, 2.2 fs. (**C**) Simplified explanation. After the compression (blue arrows), the electron wave packet (yellow) covers three sidebands (−$h\nu$, E_0, and +$h\nu$) with flat phase fronts (upper gray lines). Dispersive propagation produces nonlinear phases (lower gray lines) and interaction with the field cycles of the characterization laser (magenta arrows) becomes asymmetric because some inter-sideband couplings are more constructive (solid arrows) and others more destructive (dotted arrows). (**D**) Depiction of electron localization of a thermal emitter. Top: Hypothetical infinite coherence length. Middle: Realistic scenario with a wave packet duration σ_t of ~2.2 fs. Bottom: Electrons as point particles. Solid line, approximate electrostatic potential; Φ, work function; black arrows, propagation direction of the electrons during acceleration.

4.3 fs (dotted line), 2.7 fs (dashed line), and 2.2 fs (big dots); the last value agrees best with the data (see Fig. 3A). We conclude that randomly emitted electrons from a thermal emitter are wave functions with a few-femtosecond duration (full width at half maximum, ~5 fs) that is comparable to the laser period (6.5 fs); laser-electron interaction is therefore in a transitional regime (20, 22) between classical point-particle physics and population dynamics on a photon ladder. The results therefore confirm recent theoretical predictions of an anomalous regime in photon-induced electron microscopy for electron pulses as short as the optical cycles (22). The origin of the measured limited temporal coherence of thermal electrons may be electron localization due to temperature; invoking the time-energy uncertainty principle with an emitter temperature of $T \approx 1500$ K and the Boltzmann constant k_B produces $\hbar/(2k_BT) \approx 2.5$ fs, comparable to the measurement result.

DISCUSSION
Together, the reported data demonstrate that a continuous-wave laser can modulate the endless electron beam in a TEM into pulses of sub–light cycle duration at almost the full brightness of the source. The necessary technical modifications are rather simple (see Fig. 1B) but unify the spatial resolution provided by the electrons with the time resolution provided by the optical cycles of laser light. Percent-level sideband currents are sufficient for pulse formation in a transitional regime between classical physics and quantum mechanics. Sub–light cycle electron bunches can be transported over macroscopic distances (tens of centimeters) and through magnetic lenses of substantial magnification (>6000) without disrupting their periodicity or pulse duration. Space-time imaging or spectroscopy with photon-induced near-field electron microscopy (6), time-resolved holography (8), electron-electron diffraction (16, 17), waveform electron microscopy (9), quantum state reconstruction (23), or laser-assisted electron spectroscopy (30) may therefore be advanced to attosecond time resolution to study, for example, metamaterials, photonic integrated circuitry, solar energy convertors, or photocatalytic materials on the basis of the underlying electrodynamics in space and time. Continuous-wave laser illumination of complex materials is feasible at intensities of 10^4 to 10^6 W/cm^2 (31, 32) and with field strengths

of ~10^6 V/m, enough to produce substantial holographic image distortions (9) or spectral changes in photon-induced near-field electron microscopy (6, 31). Nanosecond excitation can be used for alleviating thermal load (33).

In contrast to femtosecond pump-probe microscopy and diffraction, which aim at tracking the evolution of a material after absorption of a femtosecond laser pulse, the main application of our electron microscopy will be investigations of electromagnetic phenomena that are triggered by the cycles of light (4) and not by the intensity envelope of pulses (1, 2). Several emerging possibilities have already been discussed by Morimoto and Baum (14) in their methods section. For example, research in nanophotonics strives for understanding and using the complex interactions of light with subwavelength structures for creating exceptional optical functionalities with metamaterials (34–39), photonic integrated circuitry (40–42), or photocatalysts (43). Waveform electron microscopy (9) with subcycle time resolution can reveal this controlled imprint of phases, amplitudes, and polarizations onto the electromagnetic field cycles of light with subwavelength and subcycle precision. If the electron beam is coherent in space, then it should also be possible to advance electron holography or picodiffraction (44, 45) to highly dynamical setting at frequencies approaching those of light, and atomic subcycle diffraction may reveal the complex real-space motions of valence electron densities that are the atomistic origin of the macroscopic optical properties of materials (16, 17). Quantum optics with free-electron wave functions (23, 46–48) and general three-body interactions of light, electrons, and matter (49) may profit from the extremely narrow spectroscopic bandwidth that is offered by a continuous laser wave (30). In cryogenic electron microscopy, the orientation of biomolecules might be identified by their optical dipole response, and a modulated electron beam in particle colliders might reveal the physics of the collisions as a function of time.

For all these endeavors, the reported subcycle transmission electron microscopy may be useful because it is complementary to existing techniques (11, 12). Future space-time investigations of electronic motion in atoms, crystals, or nanostructures will benefit from the reported concept's technical simplicity, high level of signal-to-noise ratio, and widespread applicability to complex materials of various morphology and form.

MATERIALS AND METHODS
Experimental details
The electron microscope is a Philips CM12 TEM with a LaB$_6$ electron source, aligned and set up for lowest energy spread. The energy spectrometer is a Gatan GIF 100 with an entrance aperture of 2 mm in diameter; the dispersion is set to 20 pixels/eV at the camera. The laser system is a continuous-wave, single-longitudinal-mode, thulium-doped fiber laser with a wavelength λ = 1950 nm and a line width of Δf < 50 kHz (AdValue Photonics Inc.). At the microscope, we split the laser beam in two arms of adjustable power by thin-film polarizers and half-wave plates. Additional wave plates control the polarizations. Time delay is provided by a voltage-controlled piezoelectric actuator (stack-type actuator, piezosystem jena GmbH). The modulation elements are free-standing silicon membranes (UberFlat, Norcada Inc.) with a thickness of 50 nm. Boron doping to a resistivity of <20 ohms·cm prevents electrostatic charging. The membrane for pulse compression replaces the microscope's variable condenser aperture, and the laser beam is guided through a customized aperture holder to overlap with electrons at an angle of 90° and at a beam waist of w_0 = 21 μm. The focus at the membrane is slightly elliptical with diameters ($1/e^2$) of ~40 and 80 μm, respectively. The membrane is tilted by 30.4° for velocity matching of the laser cycles with respect to the electron beam. The membrane for pulse characterization is placed at the sample position inside the twin lens. Two polished copper parallelepipeds are coated with 500 nm of gold and attached to the upper and lower magnetic pole pieces to guide the laser beam through the sample at an angle of ~30° with respect to the electrons, while the electrons have a normal angle of incidence. The laser focus has a diameter of ~40 μm ($1/e^2$). The outgoing laser beam is recorded with a camera for optimizations and diagnostics. The copper pieces do not affect the magnetic field of the twin lens in any detectable way. The data in Fig. 2A are obtained with a laser power of 3.5 W at the compression interaction and with 4.5 W at the characterization section. Peak field strengths are ~2×10^6 V/m.

Spectrometer optimizations
Energy resolution in our system is mainly limited by high-voltage drifts and magnetic fields with a prominent 50-Hz component from laboratory mains. Figure S1 depicts our approach for correcting these imperfections. We modulate the electrostatic potential inside the spectrometer prism with a three-level rectangular voltage pattern (0, 5, and 10 V) that is synchronized to the voltage oscillations of the mains. Therefore, the spectrometer collects only these electrons that pass through the whole experiment during times of low magnetic field changes (see fig. S1C). At a duty cycle of 20% (blue or green regions in fig. S1), the energy resolution improves from ~0.4 to 0.28 eV (root mean square). To eliminate slow drifts, we record, in each camera frame, always pairs of energy spectra at varying laser delay Δt (blue regions in fig. S1) together with a reference spectrum at fixed time delay (green regions in fig. S1) by synchronously alternating the rectangular voltage of the piezo-driven time delay (see fig. S1C) with the prism potential (see fig. S1B). In summary, we obtain time-delay series of drift-corrected spectra at substantially reduced influences from laboratory noise at a cost of ~80% loss in overall detection.

Electron beam
Magnification is set to ~6000. The image of the compression membrane (in its function as a condenser aperture) is projected onto the sample in such a way that there is a compromise between illumination intensity and sharpness of the image, required to create a locally flat modulation phase front at the sample in case of residual misalignments of the velocity matching. The modulated beam size at the characterization membrane is ~1 μm; therefore, the 2-mm aperture of the spectrometer collects ~$^1/_3$ of the beam diameter, that is, the inner part that is most homogeneously modulated by the laser. Temporal distortions of the magnetic lenses (27) are minimized by collinearly aligning the electron beam to the magnetic axis of all lenses (50).

Data analysis and error estimation
Data in Fig. 2A are obtained as an average of 10 scans over the desired range of time delays. Figure 2C shows data with 4 W of laser power at both interactions at a width-adding delay of 3.5 fs. Deconvolution of the signal into sidebands is performed with the Lucy-Richardson algorithm with 50 iterations and zero damping (51, 52), using a measured spectrum without laser modulation as the point-spread function. The Lucy-Richardson algorithm is well known for converging monotonically to the unique maximum-likelihood solution (51) and is widely used in astronomy, where correct evaluation of the object positions is of principal importance. The ultimate results of the deconvolution process are infinitely narrow peaks of which the positions and intensities are retrieved. Thus, the spectral width shown in Fig. 2C is arbitrary and decreases with the number of iterations, but the peak positions and their relative strengths are given by the deconvolution results (see fig. S2). To extract the delay-dependent amplitudes of the zero-loss peak A_0 and the sideband peaks $A_{\pm 1}$, we use the Levenberg-Marquardt least-square fitting algorithm with three fit parameters, $A_{\pm 1}$, and the energetic center S. The sum $A_0 + A_1 + A_{-1}$ is fixed to unity. Error levels in the reported pulse durations are estimated by the upper and lower limits of the simulation results when optimizing for different criteria of convergence (full two-dimensional pattern or deconvoluted sideband intensities as a function of time, with or without allowance for higher-order peaks, with or without normalization of the total counts). Error bars in Fig. 2G are SEs.

Definition of wave packet duration and wave packet prechirp
Our terms "wave packet duration" and "duration of the wave function" indicate the root mean square duration of the absolute square of the electron wave function in the laboratory frame. Durations as the full width at half maximum are denoted explicitly when used. In the simulations of Figs. 2 and 3, it is assumed that the initial electron wave function at the compression interaction is not chirped, that is, Fourier-limited. If a 2.2-fs-long electron wave packet is emitted from the LaB$_6$ source and travels to the compression laser interaction within ~1 ns, then it increases its duration by less than 0.2 fs; longer initial wave packets lengthen even less. Prechirp is therefore negligible and Fourier-limited wave packets can be used in the simulations.

Studies of nonlinear processes
At first glance, the repetitive nature of our electron pulses seems to prevent the study of nonlinear optical phenomena and high-field processes that are usually studied by pump-probe spectroscopy. However, the only condition is that an optical phenomenon is cycle reversible, that is, appearing reproducibly for every optical field cycle of the excitation. All linear and perturbative nonlinear optical responses in molecules, condensed matter, or nanostructures fulfill this condition,

as well as many strong-field processes, for example, optical higher-order harmonic generation in nanostructures (*38*) or multiphoton photoemission from nanoparticles (*32*). For investigations of longer-lasting phenomena, for example, cycle-by-cycle absorption of light (*17*), we can apply a midinfrared continuous-wave laser with a cycle period of tens of femtoseconds (for example, a CO_2 or quantum cascade laser) for electron pulse compression and use a locked train of femtosecond single-cycle pulses at visible or near-infrared central wavelengths for sample excitation. Dielectric membranes or related modulation elements can shape an electron beam at almost any wavelength of light (*14*); tunable lasers, multicolor fields, chirped long pulses from Fourier-domain mode locking, beams with angular momentum, or almost any other type of laser light are therefore applicable for sample excitation and synchronous production of sub–light cycle electron pulses for probing.

SUPPLEMENTARY MATERIALS

Supplementary material for this article is available at http://advances.sciencemag.org/cgi/content/full/6/46/eabb1393/DC1

REFERENCES AND NOTES

1. A. H. Zewail, Four-dimensional electron microscopy. *Science* **328**, 187–193 (2010).
2. R. J. D. Miller, Femtosecond crystallography with ultrabright electrons and x-rays: Capturing chemistry in action. *Science* **343**, 1108–1116 (2014).
3. B. J. Siwick, J. R. Dwyer, R. E. Jordan, R. J. D. Miller, An atomic-level view of melting using femtosecond electron diffraction. *Science* **302**, 1382–1385 (2003).
4. P. Baum, D. S. Yang, A. H. Zewail, 4D visualization of transitional structures in phase transformations by electron diffraction. *Science* **318**, 788–792 (2007).
5. T. Frigge, B. Hafke, T. Witte, B. Krenzer, C. Streubühr, A. Samad Syed, V. M. Trontl, I. Avigo, P. Zhou, M. Ligges, D. von der Linde, U. Bovensiepen, M. Horn-von Hoegen, S. Wippermann, A. Lücke, U. Gerstmann, W. G. Schmidt, Optically excited structural transition in atomic wires on surfaces at the quantum limit. *Nature* **544**, 207–211 (2017).
6. B. Barwick, D. J. Flannigan, A. H. Zewail, Photon-induced near-field electron microscopy. *Nature* **462**, 902–906 (2009).
7. A. Yurtsever, R. M. van der Veen, A. H. Zewail, Subparticle ultrafast spectrum imaging in 4D electron microscopy. *Science* **335**, 59–64 (2012).
8. I. Madan, G. M. Vanacore, E. Pomarico, G. Berruto, R. J. Lamb, D. McGrouther, T. T. A. Lummen, T. Latychevskaia, F. J. García de Abajo, F. Carbone, Holographic imaging of electromagnetic fields via electron-light quantum interference. *Sci. Adv.* **5**, eaav8358 (2019).
9. A. Ryabov, P. Baum, Electron microscopy of electromagnetic waveforms. *Science* **353**, 374–377 (2016).
10. N. R. da Silva, M. Moller, A. Feist, H. Ulrichs, C. Ropers, S. Schäfer, Nanoscale mapping of ultrafast magnetization dynamics with femtosecond Lorentz microscopy. *Phys. Rev. X* **8**, 031052 (2018).
11. P. B. Corkum, F. Krausz, Attosecond science. *Nat. Phys.* **3**, 381–387 (2007).
12. P. Baum, F. Krausz, Capturing atomic-scale carrier dynamics with electrons. *Chem. Phys. Lett.* **683**, 57–61 (2017).
13. K. E. Priebe, C. Rathje, S. V. Yalunin, T. Hohage, A. Feist, S. Schäfer, C. Ropers, Attosecond electron pulse trains and quantum state reconstruction in ultrafast transmission electron microscopy. *Nat. Photonics* **11**, 793–797 (2017).
14. Y. Morimoto, P. Baum, Diffraction and microscopy with attosecond electron pulse trains. *Nat. Phys.* **14**, 252–256 (2018).
15. M. Kozák, N. Schönenberger, P. Hommelhoff, Ponderomotive generation and detection of attosecond free-electron pulse trains. *Phys. Rev. Lett.* **120**, 103203 (2018).
16. H. C. Shao, A. F. Starace, Detecting electron motion in atoms and molecules. *Phys. Rev. Lett.* **105**, 263201 (2010).
17. V. S. Yakovlev, M. I. Stockman, F. Krausz, P. Baum, Atomic-scale diffractive imaging of sub-cycle electron dynamics in condensed matter. *Sci. Rep.* **5**, 14581 (2015).
18. C. Kealhofer, W. Schneider, D. Ehberger, A. Ryabov, F. Krausz, P. Baum, All-optical control and metrology of electron pulses. *Science* **352**, 429–433 (2016).
19. O. Schwartz, J. J. Axelrod, S. L. Campbell, C. Turnbaugh, R. M. Glaeser, H. Müller, Laser phase plate for transmission electron microscopy. *Nat. Methods* **16**, 1016–1020 (2019).
20. F. O. Kirchner, A. Gliserin, F. Krausz, P. Baum, Laser streaking of free electrons at 25 keV. *Nat. Photonics* **8**, 52–57 (2014).
21. Y. Morimoto, P. Baum, Attosecond control of electron beams at dielectric and absorbing membranes. *Phys. Rev. A* **97**, 033815 (2018).
22. Y. M. Pan, B. Zhang, A. Gover, Anomalous photon-induced near-field electron microscopy. *Phys. Rev. Lett.* **122**, 183204 (2019).
23. A. Feist, K. E. Echternkamp, J. Schauss, S. V. Yalunin, S. Schäfer, C. Ropers, Quantum coherent optical phase modulation in an ultrafast transmission electron microscope. *Nature* **521**, 200–203 (2015).
24. G. M. Vanacore, I. Madan, G. Berruto, K. Wang, E. Pomarico, R. J. Lamb, D. McGrouther, I. Kaminer, B. Barwick, F. J. García de Abajo, F. Carbone, Attosecond coherent control of free-electron wave functions using semi-infinite light fields. *Nat. Commun.* **9**, 2694 (2018).
25. D. F. Zhang, A. Fallahi, M. Hemmer, X. J. Wu, M. Fakhari, Y. Hua, H. Cankaya, A. L. Calendron, L. E. Zapata, N. H. Matlis, F. X. Kartner, Segmented terahertz electron accelerator and manipulator (STEAM). *Nat. Photonics* **12**, 336–342 (2018).
26. P. Baum, Quantum dynamics of attosecond electron pulse compression. *J. Appl. Phys.* **122**, 223105 (2017).
27. C. Weninger, P. Baum, Temporal distortions in magnetic lenses. *Ultramicroscopy* **113**, 145–151 (2012).
28. N. Bach, T. Domrose, A. Feist, T. Rittmann, S. Strauch, C. Ropers, S. Schäfer, Coulomb interactions in high-coherence femtosecond electron pulses from tip emitters. *Struct. Dyn.* **6**, 014301 (2019).
29. A. Feist, N. Bach, N. R. da Silva, T. Danz, M. Möller, K. E. Priebe, T. Domröse, J. G. Gatzmann, S. Rost, J. Schauss, S. Strauch, R. Bormann, M. Sivis, S. Schäfer, C. Ropers, Ultrafast transmission electron microscopy using a laser-driven field emitter: Femtosecond resolution with a high coherence electron beam. *Ultramicroscopy* **176**, 63–73 (2017).
30. E. Pomarico, I. Madan, G. Berruto, G. M. Vanacore, K. Wang, I. Kaminer, F. J. García de Abajo, F. Carbone, meV resolution in laser-assisted energy-filtered transmission electron microscopy. *ACS Photonics* **5**, 759–764 (2018).
31. C. Liu, Y. Wu, Z. Hu, J. A. Busche, E. K. Beutler, N. P. Montoni, T. M. Moore, G. A. Magel, J. P. Camden, D. J. Masiello, G. Duscher, P. D. Rack, Continuous wave resonant photon stimulated electron energy-gain and electron energy-loss spectroscopy of individual plasmonic nanoparticles. *ACS Photonics* **6**, 2499–2508 (2019).
32. M. Sivis, N. Pazos-Perez, R. Yu, R. Alvarez-Puebla, F. J. García de Abajo, C. Ropers, Continuous-wave multiphoton photoemission from plasmonic nanostars. *Commun. Phys.* **1**, 13 (2018).
33. P. Das, J. D. Blazit, M. Tencé, L. F. Zagonel, Y. Auad, Y. H. Lee, X. Y. Ling, A. Losquin, C. Colliex, O. Stéphan, F. J. García de Abajo, M. Kociak, Stimulated electron energy loss and gain in an electron microscope without a pulsed electron gun. *Ultramicroscopy* **203**, 44–51 (2019).
34. A. V. Kildishev, A. Boltasseva, V. M. Shalaev, Planar photonics with metasurfaces. *Science* **339**, 1232009 (2013).
35. X. J. Ni, Z. J. Wong, M. Mrejen, Y. Wang, X. Zhang, An ultrathin invisibility skin cloak for visible light. *Science* **349**, 1310–1314 (2015).
36. E. Maguid, I. Yulevich, D. Veksler, V. Kleiner, M. L. Brongersma, E. Hasman, Photonic spin-controlled multifunctional shared-aperture antenna array. *Science* **352**, 1202–1206 (2016).
37. M. Khorasaninejad, F. Capasso, Metalenses: Versatile multifunctional photonic components. *Science* **358**, 1146 (2017).
38. M. Sivis, M. Taucer, G. Vampa, K. Johnston, A. Staudte, A. Y. Naumov, D. M. Villeneuve, C. Ropers, P. B. Corkum, Tailored semiconductors for high-harmonic optoelectronics. *Science* **357**, 303–306 (2017).
39. G. H. Yuan, N. I. Zheludev, Detecting nanometric displacements with optical ruler metrology. *Science* **364**, 771–775 (2019).
40. J. K. Doylend, A. P. Knights, The evolution of silicon photonics as an enabling technology for optical interconnection. *Laser Photonics Rev.* **6**, 504–525 (2012).
41. J. Sun, E. Timurdogan, A. Yaacobi, E. S. Hosseini, M. R. Watts, Large-scale nanophotonic phased array. *Nature* **493**, 195–199 (2013).
42. X. Y. Xu, X. L. Huang, Z. M. Li, J. Gao, Z. Q. Jiao, Y. Wang, R. J. Ren, H. P. Zhang, X. M. Jin, A scalable photonic computer solving the subset sum problem. *Sci. Adv.* **6**, eaay5853 (2020).
43. W. B. Hou, S. B. Cronin, A review of surface plasmon resonance-enhanced photocatalysis. *Adv. Funct. Mater.* **23**, 1612–1619 (2013).
44. K. Müller, F. F. Krause, A. Béché, M. Schowalter, V. Galioit, S. Löffler, J. Verbeeck, J. Zweck, P. Schattschneider, A. Rosenauer, Atomic electric fields revealed by a quantum mechanical approach to electron picodiffraction. *Nat. Commun.* **5**, 5653 (2014).
45. W. P. Gao, C. Addiego, H. Wang, X. X. Yan, Y. S. Hou, D. X. Ji, C. Heikes, Y. Zhang, L. Z. Li, H. X. Huyan, T. Blum, T. Aoki, Y. F. Nie, D. G. Schlom, R. Q. Wu, X. Q. Pan, Real-space charge-density imaging with sub-angstrom resolution by four-dimensional electron microscopy. *Nature* **575**, 480–484 (2019).
46. R. Remez, A. Karnieli, S. Trajtenberg-Mills, N. Shapira, I. Kaminer, Y. Lereah, A. Arie, Observing the quantum wave nature of free electrons through spontaneous emission. *PRL* **123**, 060401 (2019).

47. O. Kfir, H. Lourenco-Martins, G. Storeck, M. Sivis, T. R. Harvey, T. J. Kippenberg, A. Feist, C. Ropers, Controlling free electrons with optical whispering-gallery modes. *Nature* **582**, 46–49 (2020).

48. K. Wang, R. Dahan, M. Shentcis, Y. Kauffmann, A. Ben Hayun, O. Reinhardt, S. Tsesses, I. Kaminer, Coherent interaction between free electrons and a photonic cavity. *Nature* **582**, 50–54 (2020).

49. A. Polman, M. Kociak, F. J. García de Abajo, Electron-beam spectroscopy for nanophotonics. *Nat. Mater.* **18**, 1158–1171 (2019).

50. D. Kreier, D. Sabonis, P. Baum, Alignment of magnetic solenoid lenses for minimizing temporal distortions. *J. Opt.* **16**, 075201 (2014).

51. L. B. Lucy, An iterative technique for the rectification of observed distributions. *Astron. J.* **79**, 745 (1974).

52. M. Singh, U. Tiwary, Y. Kim, Adaptively accelerated Lucy-Richardson method for image deblurring. *EURASIP J. Adv. Signal Process* **2008**, 365021 (2007).

Citation: A. Ryabov, J. W. Thurner, D. Nabben, M. V. Tsarev, P. Baum, Attosecond metrology in a continuous-beam transmission electron microscope. *Sci. Adv.* **6**, eabb1393 (2020).

Science Advances

Attosecond metrology in a continuous-beam transmission electron microscope

A. Ryabov, J. W. Thurner, D. Nabben, M. V. Tsarev and P. Baum

ARTICLE TOOLS	http://advances.sciencemag.org/content/6/46/eabb1393
SUPPLEMENTARY MATERIALS	http://advances.sciencemag.org/content/suppl/2020/11/09/6.46.eabb1393.DC1
REFERENCES	This article cites 52 articles, 14 of which you can access for free http://advances.sciencemag.org/content/6/46/eabb1393#BIBL
PERMISSIONS	http://www.sciencemag.org/help/reprints-and-permissions

Use of this article is subject to the Terms of Service